



A dielectric study of Br-doped lead-free methylammonium bismuth chloride $(\text{CH}_3\text{NH}_3)_3\text{Bi}_2\text{Br}_x\text{Cl}_{9-x}$

Paramesh Chandra¹ · Saroj Saha¹ · Swapan K. Mandal¹

Received: 23 January 2022 / Accepted: 9 May 2022

© The Author(s), under exclusive licence to Springer-Verlag GmbH, DE part of Springer Nature 2022

Abstract

We report here the synthesis and dielectric characteristics of lead-free methylammonium bismuth chloride (MABiCl) and bromine (Br) doped methylammonium bismuth chloride (MABiBrCl) powders. The dielectric characteristics of the samples (pressed powder pellet) measured in the frequency range 1 Hz to 1 MHz and temperature range 333–403 K indicate complex electrical transport in these halide perovskite materials. We have observed that the transport is dominated by long-range hopping of carriers and localized charges above and below a critical frequency respectively. The experimental data are fitted with the theoretical models considering grains, grain boundary, and contacts effects and made a comprehensive analysis. The activation energy obtained from ac electrical conductivity measurements is found to be relatively higher for the Br doped MABiBrCl than undoped MABiCl, which might explain some of the properties reported on solar cells and optoelectronic devices.

Keywords Perovskite · Chemical synthesis · Impedance spectroscopy · Dielectric relaxation

1 Introduction

Metal–organic hybrid perovskite with the general formula of AMX_3 (A = organic group; M = metal ion and X = halide ions) has proven its potential in the field of optoelectronics and photovoltaic applications [1–8]. Although $\text{CH}_3\text{NH}_3\text{PbX}_3$ perovskites are the most used materials for solar cell fabrication, low stability, high sensitivity towards moisture and the occurrence of highly poisonous lead (Pb) curb their development [9]. There are attempts to replace Pb with Sn but the compound such as MASnI_3 , FASnI_3 rapidly oxidized from Sn^{2+} to Sn^{4+} under ambient conditions. Another promising cation to replace Pb^{2+} (electron configuration (Xe) $4f^{14}5d^{10}6s^26p^2$) is Bi^{3+} (electron configuration (Xe) $4f^{14}5d^{10}6s^26p^3$) with similar electronic configuration and ionic radii, and with better stability than Sn^{2+} and Ge^{2+} [10, 11]. Bi^{3+} being a heavy metal cation, band dispersion due to spin–orbit coupling is expected. In addition, Bi^{3+} similar to Pb^{2+} is also a cation with high polarization and possesses a high-Born effective charge, which leads to high dielectric

constants that are important for increased screening of charged defects [12]. However, bismuth-based perovskite solar cell is incapable to achieve good efficiency till now [10, 11, 13] compared to other lead-free perovskite solar cells which can be due to poor surface morphology, low carrier diffusion length and high defect. So, extensive research is being conducted by numerous researchers to substitute Pb in the perovskite to achieve higher efficiency and stability.

Tunability of organic–inorganic perovskite (ABX_3) that can be easily explored by replacing A, the organic cation, B, the metal cation, or X, the halogen anion, or by including a small amount of dopants. Previous works have highlighted that bromine (Br) doping substantially improves the charge carrier lifetime of lead-based perovskites [13]. Another report highlighted the positive aspect of Br doping in Pb-based perovskites results in improved carrier mobility along with photovoltaic parameters such as V_{oc} , J_{sc} and FF [14].

In hybrid halide perovskites, the charge transport properties which eventually determine the performance of a solar cell device are very much dependent on the microstructure, grains and grain boundaries and most importantly the interface between the dielectric and the electrode contacts. Impedance spectroscopy (IS) is very useful to obtain and analyse the electrical properties of the dielectric medium (perovskite here). This technique models the dielectric

✉ Swapan K. Mandal
sk_mandal@hotmail.com

¹ Department of Physics, Visva-Bharati, Santiniketan 731 235, India

medium as an equivalent circuit consisting of capacitance, inductance and resistance and therefore the dielectric response in terms of dynamical properties (capacitance, conductance, permittivity, and loss factor) of the materials. The underlying basic physical processes giving rise to a large dielectric relaxation in halide perovskite photovoltaic devices need to be understood [15]. The charge transport properties of perovskite are due to electrons and holes rather than the bound excitons in the absorber [16, 17]. A clear perception till date is missing and therefore, we have tried here to understand the mechanism of dielectric relaxation in these halide perovskites using impedance spectroscopy and the role of the halide ion on the physical properties. In this study, we will report the synthesis and the dielectric properties of lead-free methylammonium bismuth chloride (MABiCl) and Br-doped methylammonium bismuth chloride (MABiBrCl).

2 Experimental details

2.1 Chemicals

The raw materials for the synthesis of the perovskite material were methylamine, hydrochloric acid (HCl, Merck Chemicals), hydrobromic acid (HBr, Merck Chemicals), anhydrous N, N dimethylformamide (DMF) ($\text{C}_3\text{H}_7\text{NO}$, Merck Chemicals, 99.5%). All the chemicals were taken of analytical grade purity and without purification.

2.2 MABiCl synthesis

$\text{CH}_3\text{NH}_3\text{Cl}$ (MACl) was produced by reacting a 1:1 ratio of methylamine (33 wt% in ethanol) and hydrochloric acid (35%) in absolute ethanol in ice at 0 °C for 2 h with constant stirring. We found a clear solution, which was allowed to evaporate slowly keeping the bath temperature at 50 °C. After that, the ethanol was slowly evaporated under continuous stirring at a constant temperature 50 °C in a vacuum for 24 h. This process results in a white precipitate of MACl.

Synthesis of the lead-free Bi-based perovskite (CH_3NH_3)₃Bi₂Cl₉ (MABiCl) was done by mixing 3:2 molar amount $\text{CH}_3\text{NH}_3\text{Cl}$ (10 mmol) and BiCl₃ (6.66 mmol) in DMF. The solution is stirred for half an hour at 50 °C resulting in a white foggy white solution. The addition of 20 ml of ethyl alcohol resulted in the formation of a white precipitate. The solution is filtered and dried at 60 °C in vacuum condition to get MABiCl powder.

2.3 MABiBrCl synthesis

$\text{CH}_3\text{NH}_3\text{Br}$ (MABr) was synthesized by reacting a 1:1 ratio of methylamine (33 wt% in ethanol) and hydrobromic acid

(35%) in absolute ethanol in ice at 0 °C for 2 h under stirring condition. A clear solution was found, which was allowed to evaporate slowly keeping the bath temperature at 50 °C. After that, the ethanol was slowly evaporated under continuous stirring at a constant temperature 50 °C in a vacuum for 24 h. The evaporation of ethanol results in a white precipitate of MABr.

Synthesis of the Bi-based perovskite (CH_3NH_3)₃Bi₂Br₃Cl₆ (MABiBrCl) was done by mixing 3:2 molar amount $\text{CH}_3\text{NH}_3\text{Br}$ (10 mmol) and BiCl₃ (6.66 mmol) in DMF. The solution is stirred for half an hour at 50 °C resulting in a white foggy solution. The addition of ethyl alcohol resulted in the formation of a white precipitate. 20 ml ethyl alcohol is added to get a white precipitate. The solution is filtered and dried under a constant 60 °C in the vacuum condition to get MABiBrCl powder.

For dielectric measurement, we used pelletized samples (diameter ~ 8 mm and thickness ~ 1.1 mm). Prepared powder samples are pressed for 5 min with applied pressure ~ 5 ton using a hydraulic pellet press system. After that, the pellets are sintered for 30 min at 100 °C. Electrical contacts on both sides of the sample are prepared by depositing a thin layer of silver (Ag). The samples are further dried at moderate temperature (between 40 and 50 °C) in ambient condition. The dielectric measurements are carried out for two pelletized samples of MABiCl and MABiBrCl.

3 Material characterization

Scanning electron microscopy (SEM ZEISS GEMINI SEM 450) was used to study the morphology of the MABiCl and MABiBrCl samples. To measure the complex impedance, the pelletized sample of MABiCl and MABiBrCl has been inserted between two copper electrodes and all data have been recorded using Hioki LCR Q (LM3536) meter. The crystal structure of the sample is obtained by synchrotron x-ray diffraction (INDUS-II Grazing Incidence X-ray Scattering (GIXS) Beam Line No.-13, RRCAT Indore). A scintillation detector (C400, Oxford Instruments) is attached to the goniometer's detection arm with a crossed slit assembly.

4 Results and discussion

4.1 XRD analysis

Figure 1a, b show the XRD pattern of the MABiCl and MABiBrCl sample respectively. The characteristic diffraction peaks are indexed using the CIF file of the previously published literature [18]. The XRD pattern for both the samples depicts a monoclinic structure with P21/n symmetry. We observed a small shift in some peaks which may be

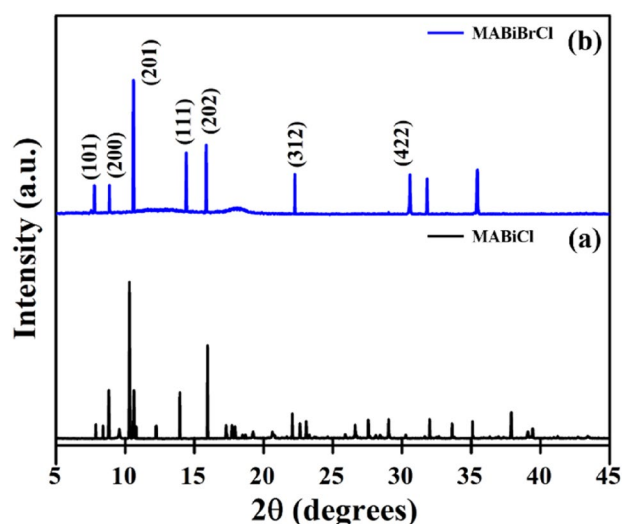


Fig. 1 X-Ray diffraction (XRD) pattern for **a** $(\text{CH}_3\text{NH}_3)_3\text{Bi}_2\text{Cl}_9$ (MABiCl) and **b** $(\text{CH}_3\text{NH}_3)_3\text{Bi}_2\text{Br}_x\text{Cl}_{9-x}$ ($x=3$) (MABiBrCl)

attributed to the micro-strain developed due to difference in ionic radii of Br and Cl ions.

4.2 FESEM analysis

The morphological structure of MABiCl and MABiBrCl samples is shown in Fig. 2a, b respectively. It is observed that the microstructure contains disc-like flakes ranging from 100 nm to 5 μm . Br doping tends to produce a bending

Fig. 2 SEM image of **a** $(\text{CH}_3\text{NH}_3)_3\text{Bi}_2\text{Cl}_9$ (MABiCl) and **b** $(\text{CH}_3\text{NH}_3)_3\text{Bi}_2\text{Br}_x\text{Cl}_{9-x}$ ($x=3$) (MABiBrCl)

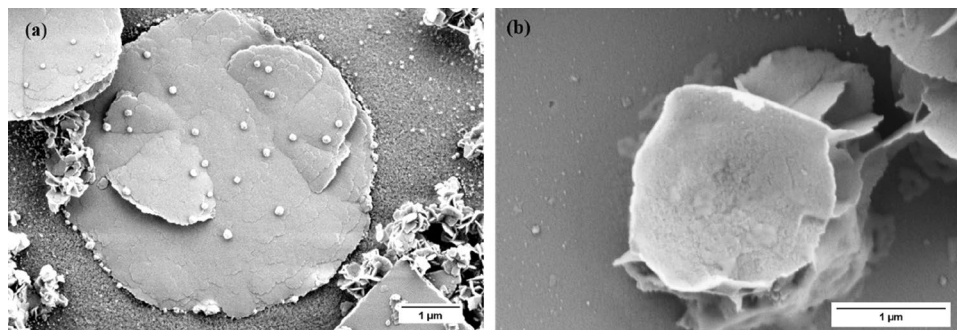
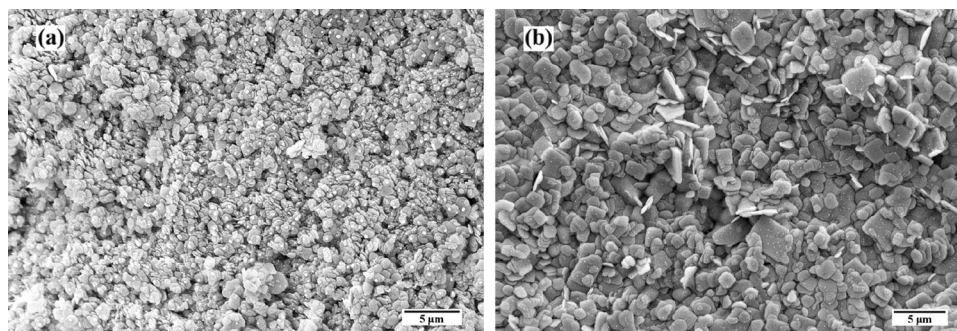


Fig. 3 Large scale view of SEM morphology of the pelletized sample of **a** MABiCl and **b** MABiBrCl



on the edge of the disc-like shapes. Figure 3a, b present the large-scale image of MABiCl and MABiBrCl pellets. Br doped sample shows a visible increase ($\sim 100\text{--}300\text{ nm}$) in grain size. Energy dispersive x-ray (EDX) spectrum (not shown here) of both the samples also confirms the presence of individual elements.

4.3 Impedance spectroscopy

The frequency and temperature dependent dielectric properties of the synthesized perovskites $(\text{CH}_3\text{NH}_3)_3\text{Bi}_2\text{Cl}_9$ and $(\text{CH}_3\text{NH}_3)_3\text{Bi}_2\text{Br}_x\text{Cl}_{9-x}$ ($x=3$) referred as MABiCl and MABiBrCl respectively have been studied with complex impedance spectroscopy in terms of complex impedance, complex permittivity, complex electric modulus and the loss tangent. The frequency ω is varied in the range of 1 Hz to 1 MHz whereas the temperature T is varied from 333 to 403 K. The frequency-dependent impedance can be expressed as

$$Z(\omega) = Z'(\omega) + iZ''(\omega) \quad (1)$$

Figure 4a, c shows the variation of the real part (Z') of complex impedance with frequency and Fig. 4b, d presents the variation of the imaginary part of impedance $Z''(\omega)$ with frequency at different temperatures for both MABiCl and MABiBrCl samples respectively. The complex impedance is expressed as $Z' - iZ'' = R_s - i/\omega C_s$ where R_s and C_s are the series resistance and capacitance respectively. We

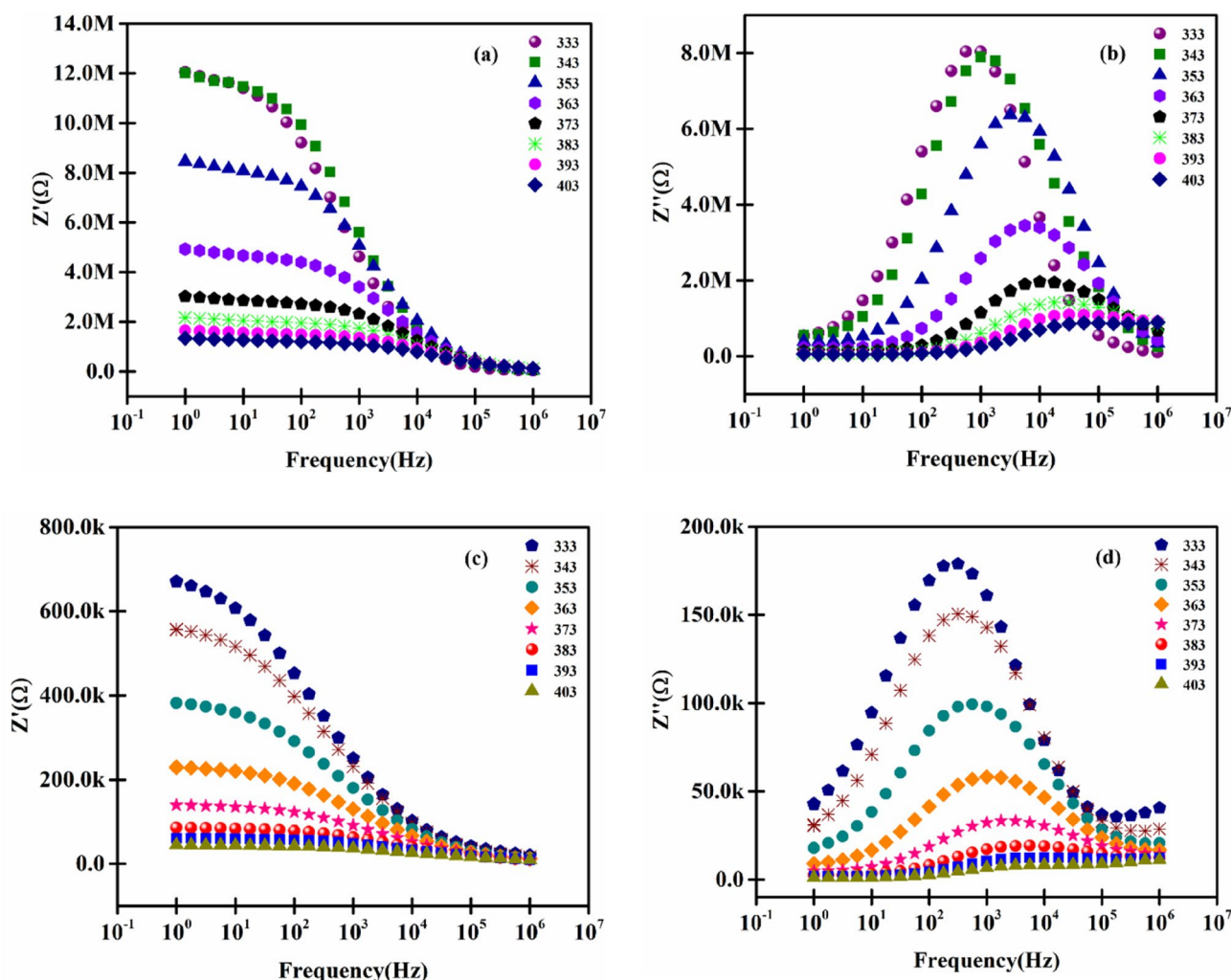


Fig. 4 Impedance spectroscopy of MABiCl and MABiBrCl at different temperatures (in the range 333 K–403 K). **a** Real part of impedance vs. frequency for sample MABiCl, **b** imaginary part of impedance vs. frequency for sample MABiCl, **c** Real part of impedance vs. frequency for sample MABiBrCl, **d** imaginary part of impedance vs. frequency for sample MABiBrCl

find that Z' decreases with the increase in frequency as well as temperature and indicates the negative temperature coefficient of resistance (NTCR)-type behaviour for both the samples [19, 20]. The Z'' data further shows a distinct peak corresponding to a relaxation frequency and the peak is found to be shifted to higher frequency with increasing temperature indicating thermal dependence of the relaxation process. The broadening of the peak is indicative of a divergence from an ideal Debye-type. Furthermore, reduction of the peak height with temperature is also observed.

Figure 5a, b shows the Cole–Cole plots (Nyquist plots) of the complex impedance Z'' vs Z' at various temperatures for the samples MABiCl and MABiBrCl respectively. The Cole–Cole plot shows semicircular arcs and is modelled by an equivalent circuit consisting of parallel RC combinations as shown in Fig. 6. We observed that the radii of the semicircles decrease with increasing temperature which

confirms again the NTCR behaviour of both the materials [20, 21].

In most cases, for a dielectric material, three distinct semicircles appear in the Nyquist diagram. These three semicircles are primarily due to the contributions of electrode–material interface, grain, and grain boundary. Semicircle in high-frequency region is attributed to the contribution of grains and that of in the low-frequency region is assigned to the contribution from the grain boundaries and the electrode–material interface. The real $Z'(\omega)$ and imaginary $Z''(\omega)$ parts of impedance can be given by:

$$Z'(\omega) = \frac{R_g}{[1 + (\omega R_g C_g)^2]} + \frac{R_{gb}}{[1 + (\omega R_{gb} C_{gb})^2]} + \frac{R_c}{[1 + (\omega R_c C_c)^2]} \quad (2)$$

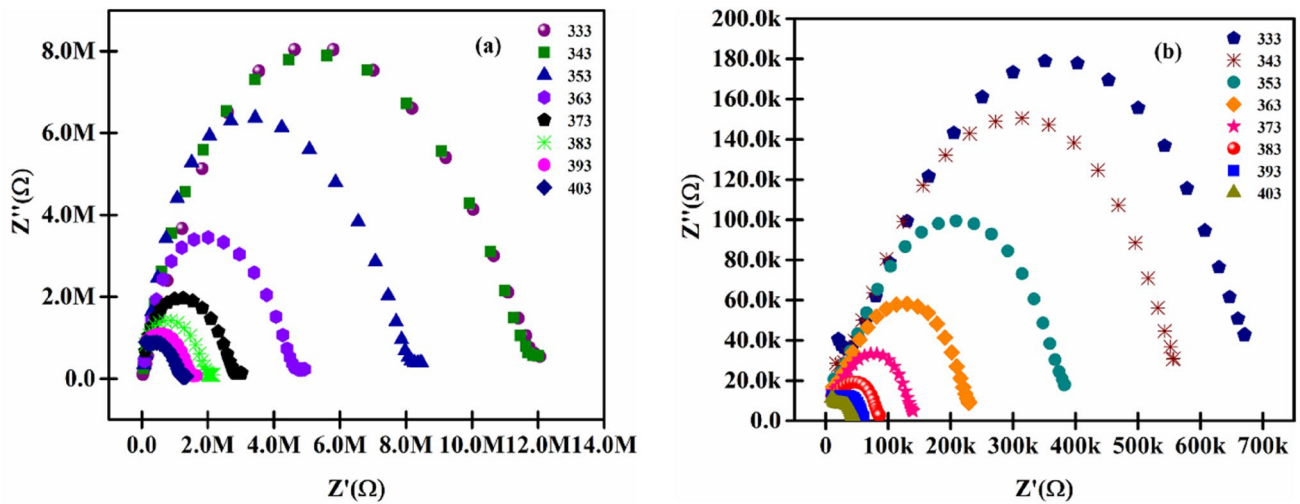


Fig. 5 Cole–Cole plot for **a** MABiCl sample and **b** MABiBrCl sample

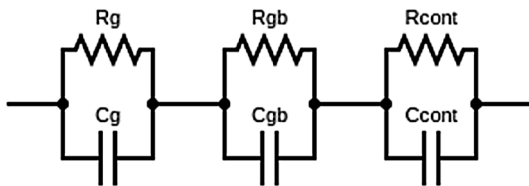


Fig. 6 Equivalent circuit diagram

$$Z''(\omega) = \frac{C_g R_g}{[1 + (\omega R_g C_g)^2]} + \frac{\omega C_{gb} R_{gb}}{[1 + (\omega R_{gb} C_{gb})^2]} + \frac{\omega C_c R_c}{[1 + (\omega R_c C_c)^2]} \quad (3)$$

Tables 1 and 2 show the calculated values for R_{cont} , R_{gb} , R_g , and C_{cont} , C_{gb} , C_g for samples MABiCl and MABiBrCl respectively. Temperature variation of R_{cont} , R_{gb} , R_g and C_{cont} , C_{gb} , C_g is shown in Fig. 7a, b for sample MABiCl and that of sample MABiBrCl in Fig. 8a, b. Both the samples show

Table 1 Calculated values of various charge transfer parameters (R_{cont} , C_{cont} , R_{gb} , C_{gb} , R_g) of MABiCl

$T(K)$	$R_{\text{cont}}(\text{M}\Omega)$	$C_{\text{cont}}(\text{pF})$	$R_{\text{gb}}(\text{M}\Omega)$	$C_{\text{gb}}(\text{pF})$	$R_g(\text{M}\Omega)$	$C_g(\text{pF})$
333	0.245	109	0.277	4.21	0.126	0.208
343	0.202	99.5	0.225	4.05	0.112	0.220
353	0.136	101	0.154	3.85	0.079	0.192
363	0.081	85.6	0.093	2.99	0.047	0.127
373	0.049	74.9	0.056	2.45	0.030	0.085
383	0.028	73.2	0.033	2.35	0.021	0.072
393	0.019	74.5	0.021	2.47	0.018	0.063
403	0.013	86.5	0.014	2.97	0.015	0.060

Table 2 Calculated values of various charge transfer parameters (R_{cont} , C_{cont} , R_{gb} , C_{gb} , R_g) of MABiBrCl

$T(K)$	$R_{\text{cont}}(\text{M}\Omega)$	$C_{\text{cont}}(\text{pF})$	$R_{\text{gb}}(\text{M}\Omega)$	$C_{\text{gb}}(\text{pF})$	$R_g(\text{M}\Omega)$	$C_g(\text{pF})$
333	5.78	2810	12.6	162	9.46	30.3
343	8.75	638	13.2	49.7	7.7	8.3
353	6.43	396	7.18	4.83	10.3	28.9
363	3.67	349	5.64	26.5	3.75	4.34
373	2.49	216	3.3	17.1	2.08	2.35
383	1.81	165	2.37	13	1.81	1.36
393	1.32	158	1.82	12	1.74	0.951
403	0.92	197	1.45	12.9	1.63	0.830

Fig. 7 Plot of the variation of **a** R_{cont} , R_{gb} , R_{g} and **b** that of C_{cont} , C_{gb} , C_{g} with temperature for sample MABiCl

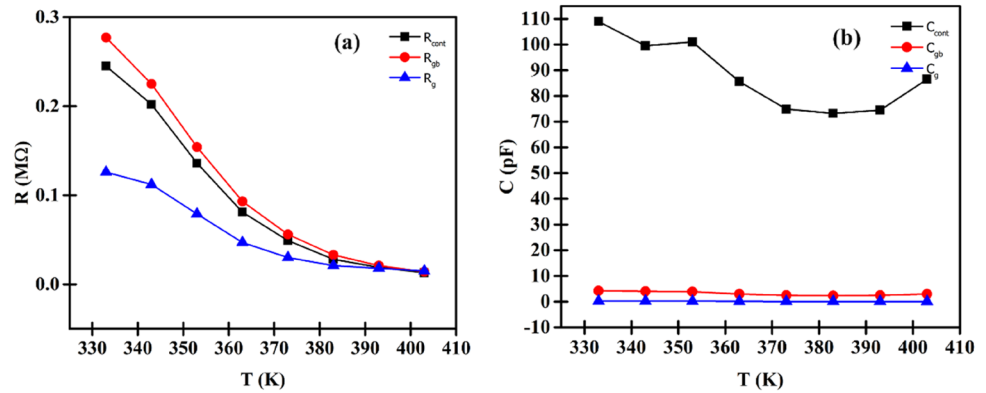
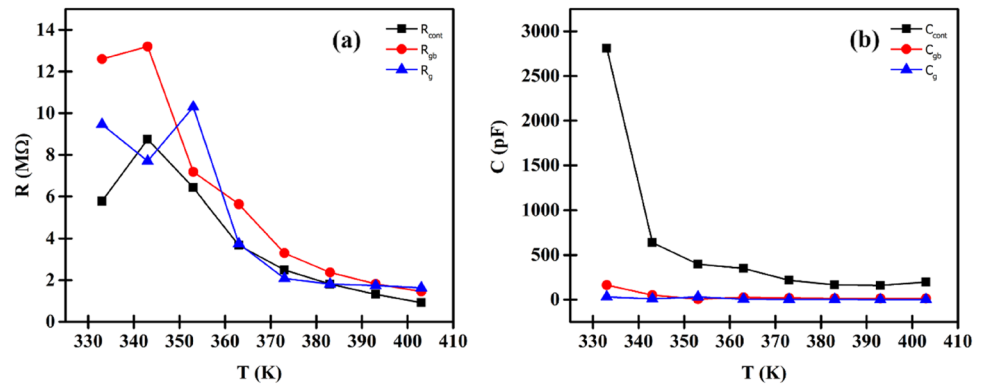


Fig. 8 Plot of the variation of **a** R_{cont} , R_{gb} , R_{g} and **b** that of C_{cont} , C_{gb} , C_{g} with temperature for sample MABiBrCl



that the resistance decreases with increasing temperature and eventually reaches a saturation value. In the case of capacitive contribution, the C_{cont} value for both samples decrease with temperature whereas C_{gb} and C_{g} remain almost constant. Diffusion of contact material (Ag) inside the perovskite material may be the reason behind the higher value of resistance for contact electrode, and deviation from its ideal metallic property for temperature variation.

4.4 Dielectric permittivity

Upon application of an external oscillating electric field in a given frequency range, the dielectric behaviour of MABiCl and MABiBrCl can be studied by the complex permittivity. The frequency-dependent complex dielectric permittivity can be expressed as:

$$\varepsilon(\omega) = \varepsilon'(\omega) - j\varepsilon''(\omega) \quad (4)$$

where the real part $\varepsilon'(\omega)$ defines the charge storing capacity and the imaginary part $\varepsilon''(\omega)$ indicates the energy loss within the material [21–24]. $\varepsilon'(\omega)$ and $\varepsilon''(\omega)$ have been determined using Eqs. (5) and (6):

$$\varepsilon'(\omega) = \frac{Z''}{\omega C_0 (Z'^2 + Z''^2)} \quad (5)$$

$$\varepsilon''(\omega) = \frac{Z'}{\omega C_0 (Z'^2 + Z''^2)} \quad (6)$$

where $\omega = 2\pi f$ is the angular frequency and $C_0 = \varepsilon_0 \frac{A}{t}$ (in which ε_0 is the free space permittivity, and A and t are the cross-sectional area and thickness of the pellet, respectively). Unlike insulators where the relaxation mechanism is majorly influenced by the frequency-dependent part of the impedance value, semiconductors consist of frequency-independent DC conductivity which complicates any relaxation process [25–27]. Figure 9a, c shows the variation of $\varepsilon'(\omega)$ with frequency for sample MABiCl and MABiBrCl respectively. The variation of dielectric loss $\varepsilon''(\omega)$ with frequency is shown in Fig. 9b, d. Koop's phenomenological theory based on the Maxwell–Wagner model can be used to demonstrate the frequency-dependent behaviour of $\varepsilon'(\omega)$ and $\varepsilon''(\omega)$ [20, 28–30]. In this theory, the material is considered to be an inhomogeneous medium consisting of grains separated by definite boundaries with negligible conduction or high potential barriers. Under the influence of an applied alternating electric field, the electrons move toward the grain boundary by the hopping mechanism. Now, if the resistance is massive enough at the grain boundary, then the electrons may accumulate at the grain boundaries and produce polarization. But as the frequency increases the electron hardly copes up with rapid force field direction alteration which in

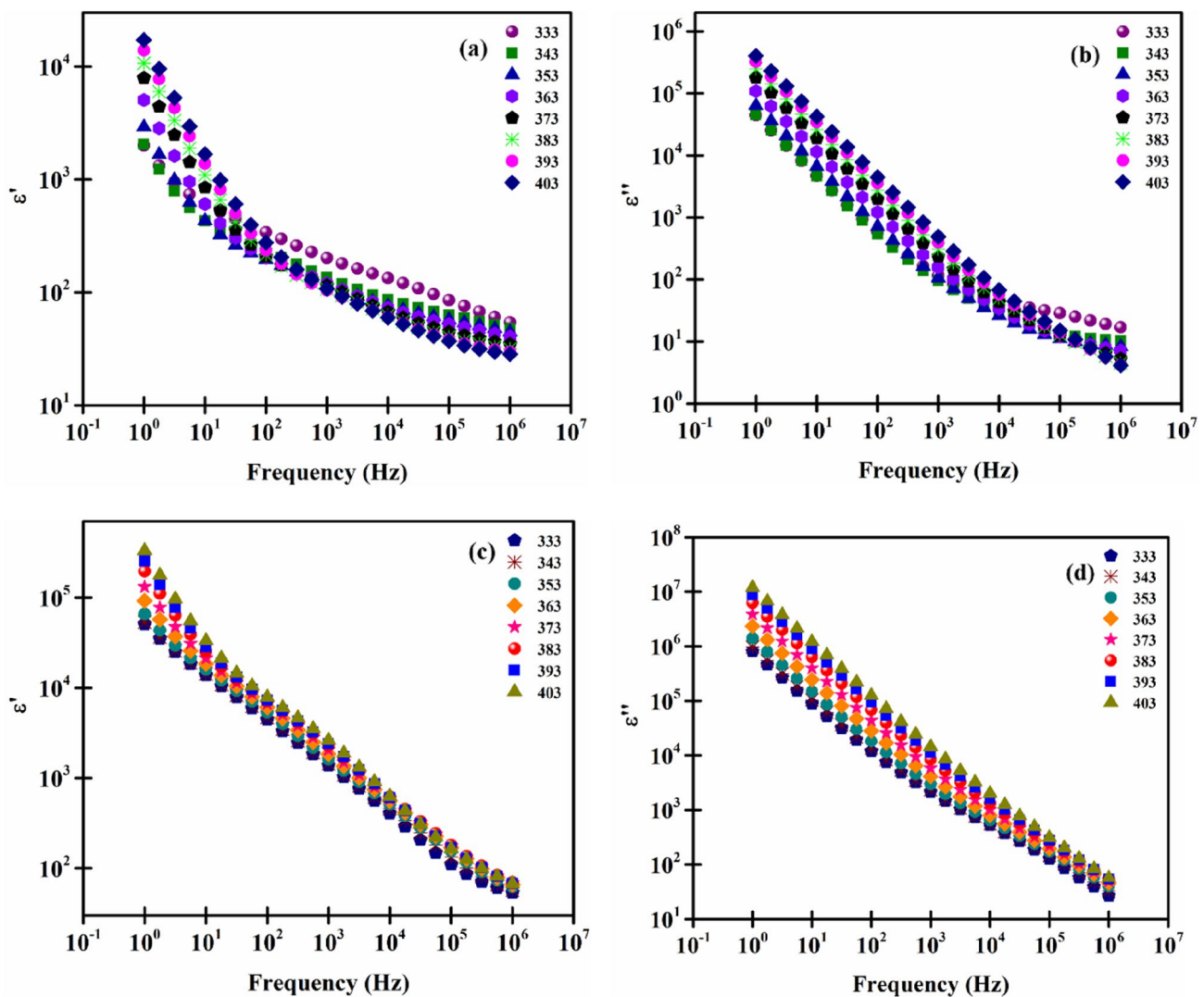


Fig. 9 Frequency-dependent plot of the real and imaginary parts of $\epsilon(\omega)$. **a** real part $\epsilon'(\omega)$, **b** imaginary part of $\epsilon''(\omega)$ for MABiCl and **c** real part $\epsilon'(\omega)$ and **d** imaginary part $\epsilon''(\omega)$ of MABiBrCl

turn reverses the electron flow and decrease in polarization [31–33]. The ionic polarization within the material arises due to the separation of negative $(\text{Bi}_2\text{X}_9)^{3-}$ and positive MA^+ charge centres. Higher values of $\epsilon'(\omega)$ at low frequencies may be attributed to the contribution of ionic polarization within the material.

4.5 Dielectric modulus

The relaxation mechanism of MABiCl and MABiBrCl has been also analysed in terms of dielectric modulus. Dielectric modulus can be stated as Eq. (7)

$$M(\omega) = M'(\omega) + jM''(\omega) = \frac{1}{\epsilon(\omega)} = \frac{\epsilon'(\omega)}{(\epsilon'^2 + \epsilon''^2)} + j\frac{\epsilon''(\omega)}{(\epsilon'^2 + \epsilon''^2)} \quad (7)$$

where $M'(\omega)$ is the real part and $M''(\omega)$ is the imaginary part of dielectric modulus. Figure 10a–d shows the temperature and frequency variation of $M'(\omega)$ and $M''(\omega)$ in the temperature range 333 K–403 K and frequency range 1 Hz to 1 MHz for MABiCl and MABiBrCl. For lower frequency range, $M'(\omega)$ almost vanishes for both MABiCl and MABiBrCl. Figure 10b, d shows that $M''(\omega)$ vs. frequency curve shifts downward with the increasing temperature in the low-frequency region and shifts upward with increasing temperature in the high-frequency region, which may be attributed to the presence of the short-range and long-range mobility of charge carriers inside the material MABiCl and MABiBrCl for different frequency ranges. $M''(\omega)$ value depicted the dielectric loss for MABiCl and MABiBrCl [28]. The relaxation phenomenon inside both materials gives rise to a characteristic peak (f_{max}) which tends to shift toward

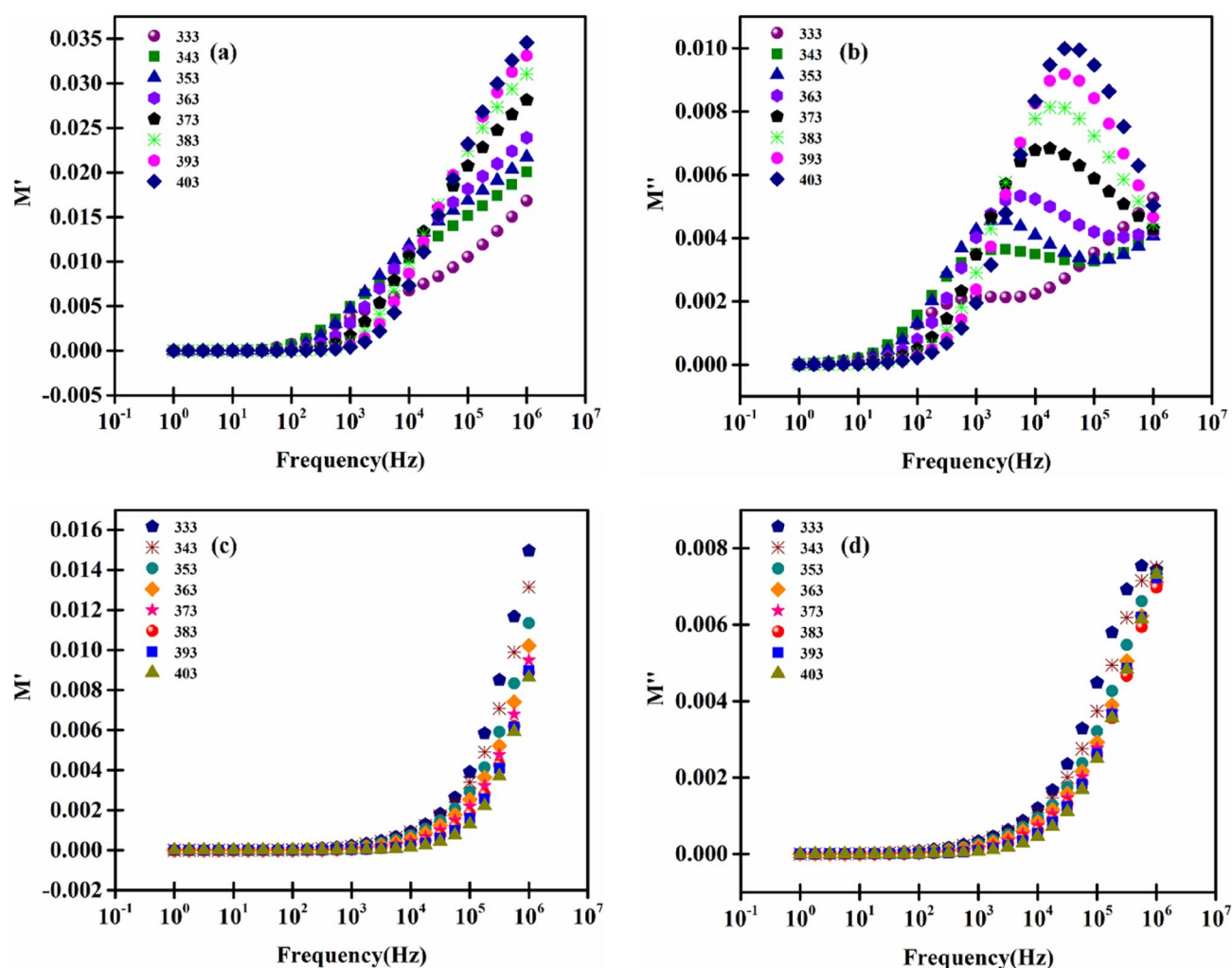


Fig. 10 Logarithmic angular frequency dependence of M' and M'' **a, b** of MABiCl and **c, d** of MABiBrCl

higher frequencies with the increase in temperature which can be caused by the movement of free charges generated by thermal energy. The frequency variation of $M''(\omega)$ below f_{\max} is correlated to the hopping of mobile charge carriers over a long range inside the MABiCl and MABiBrCl and above f_{\max} to the short-range or localized motion of charge carriers. An increase in grain size for Br doped sample plausibly gives rise to the observed shift of f_{\max} for MABiBrCl sample. The relaxation peak points to the transition from the long-range to the short-range mobilization of free charges in MABiCl and MABiBrCl. For MABiCl the characteristic frequency tends to move towards a higher frequency from 10^2 to 10^5 Hz but in the case of MABiBrCl characteristic frequency starts from $>10^5$ Hz and goes out of the frequency range (greater than 10^6 Hz) of our experimental setup with increasing temperature. We can deduce that the MABiBrCl sample shows the long-range electron hopping for a greater range

of frequency values and the range increases with increasing temperature.

4.6 AC electric conductivity

AC electrical conductivity appears to be a suitable technique to probe different dielectric relaxation mechanisms in a complex material like halide perovskites. The material may consist of charged species like molecules, ions, electrons, or holes. Response to these charged species upon application of an electric field eventually determines the photovoltaic response of the material. The frequency (ω) dependent electrical conductivity is usually characterized by Jonscher's power law [34] presented in Eq. (8):

$$\sigma(\omega) = \sigma_{dc} + A\omega^n \quad (8)$$

where σ_{dc} is the dc conductivity, A is a temperature dependent constant, and n being the frequency exponent (between 0 and 1). At low frequency, the electrical conductivity is nearly equal to the dc conductivity, which does not change significantly up to a critical frequency and is arising out of long-range hopping of charge carriers due to resistive grain boundaries. Beyond the critical frequency, as the frequency is increased, the conductivity increases nonlinearly. This is ascribed to the short-range hopping of charge carriers dominated by trap-controlled ac electrical conduction process. Perovskites are often characterised by the presence of traps within the semiconducting bandgap. This is often described by a jump relaxation model (JRM model) to account for the dispersive nature of the conductivity at high frequency. The electrical conductivity is calculated from the relation $\sigma = \omega \epsilon_0 \epsilon''$, where ϵ_0 is the permittivity of free space. In Fig. 11a, c, we plot the measured AC electrical

conductivity of MABiCl and MABiBrCl in the frequency range 1 Hz–1 MHz. The data shows two distinct regimes of the conductivity below and above the critical frequency, also called the hopping frequency (ω_p), corresponding to the long range and short-range hopping of carriers respectively, as discussed above.

Here, for all temperatures, the result shows that σ_{dc} follows the Arrhenius relation (Eq. 9):

$$\sigma_{dc} = \sigma_0 \exp\left(-\frac{E_a}{KT}\right) \quad (9)$$

where σ_0 is the pre-exponential factor, E_a represents activation energy, K is the Boltzmann constant, and T is the absolute temperature [29–31]. The activation energies are obtained from the Arrhenius plot as shown in Fig. 11b, d, and the values are 0.326 eV and 0.538 eV for MABiCl and

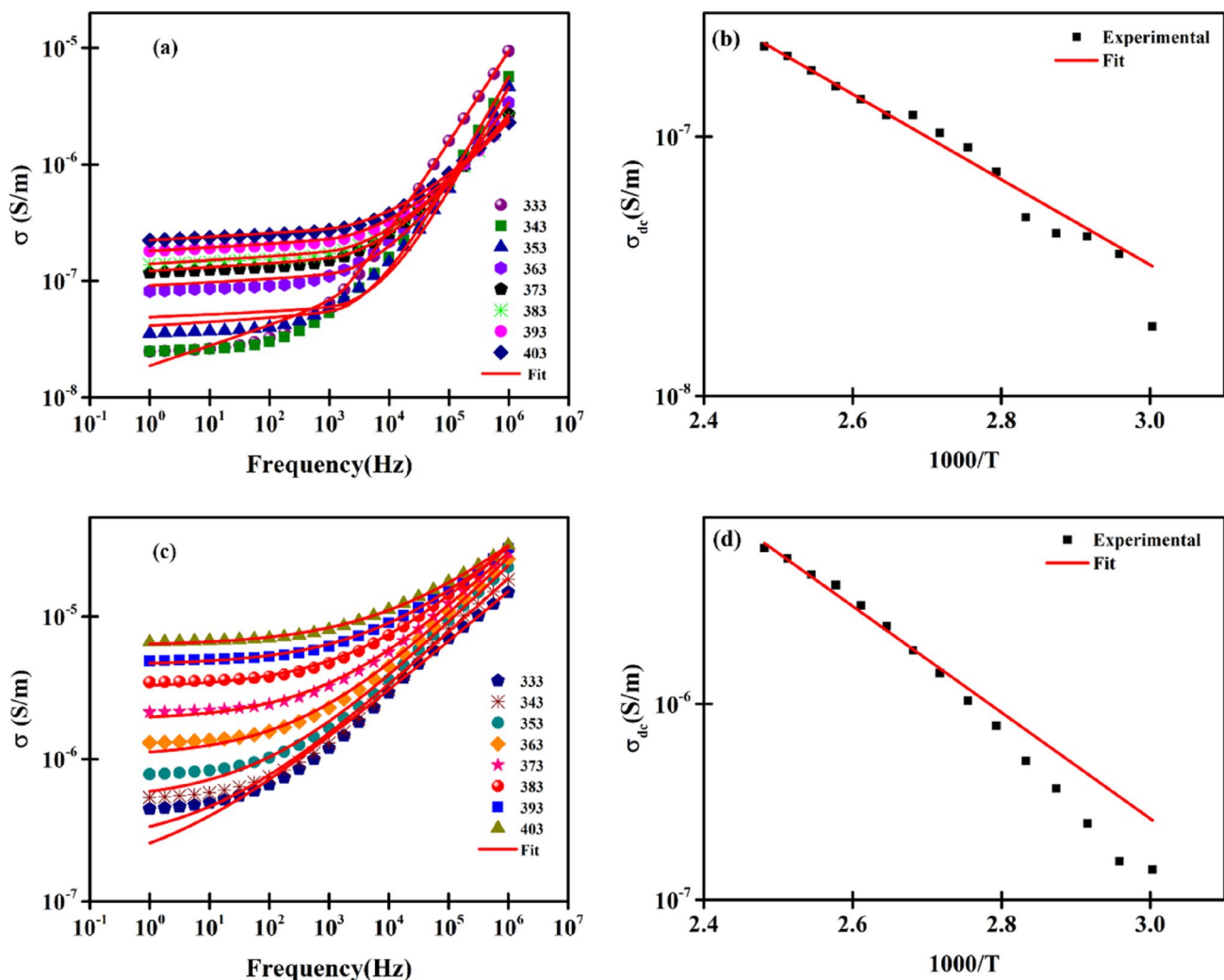


Fig. 11 **a** Electrical conductivity vs. frequency plot for temperature range 333–403 K for MABiCl and **b** Arrhenius plot of MABiCl. **c** Electrical conductivity vs. frequency plot from temperature 333–403 K and **d** Arrhenius plot of MABiBrCl

MABiBrCl respectively. It's evident from the values of activation energy that the MABiBrCl sample shows higher activation energy which may explain some of the properties of perovskite materials.

5 Conclusion

In summary, dielectric behaviours of MABiCl and MABiBrCl samples have been reported here. Frequency and temperature-dependent electrical transport properties based on dielectric studies reveal complex characteristics of these hybrid perovskite materials. The obtained experimental results are further analysed with theoretical models considering the probable contribution of the electrical contact, grains, and grain boundaries which eventually modified the relaxation of carriers within the perovskite material. We also noticed that the activation energy is relatively higher for the Br-doped MABiBrCl than MABiCl, which might explain some of the properties reported on solar cells and optoelectronic devices.

Acknowledgements The author Paramesh Chandra acknowledges with thanks to DST-PURSE, Visva-Bharati for providing research fellowship. CSIR, Govt. of India is also acknowledged with thanks by Saroj Saha for providing a Senior Research Fellowship. We also acknowledge UGC-DAE, Indore for providing us with the dielectric measurement facilities.

Data availability The author confirms that all data generated and analysed during this study are included in this article. Furthermore, all sources used to correlate the study are properly referenced or publicly available at the time of submission.

Declarations

Conflict of interest The authors declare that they have no conflict of interest.

References

1. A. Kojima, K. Teshima, Y. Shirai, T. Miyasaka, *J. Am. Chem. Soc.* **131**, 6050 (2009)
2. J.M. Azpiroz, E. Mosconi, J. Bisquert, F. De Angelis, *Energy Environ. Sci.* **8**, 2118 (2015)
3. T.Y. Yang, G. Gregori, N. Pellet, M. Grätzel, J. Maier, *Angew. Chemie - Int. Ed.* **54**, 7905 (2015)
4. S.S. Shin, E.J. Yeom, W.S. Yang, S. Hur, M.G. Kim, J. Im, J. Seo, J.H. Noh, S. Il-Seok, *Science* **356**, 167 (2017)
5. Q. Jiang, L. Zhang, H. Wang, X. Yang, J. Meng, H. Liu, Z. Yin, J. Wu, X. Zhang, J. You, *Nat. Energy* **2**, 16177 (2016)
6. T. Jesper-Jacobsson, J.P. Correa-Baena, M. Pazoki, M. Saliba, K. Schenk, M. Grätzel, A. Hagfeldt, *Energy Environ. Sci.* **9**, 1706 (2016)
7. W.S. Yang, J.H. Noh, N.J. Jeon, Y.C. Kim, S. Ryu, J. Seo, S. Il-Seok, *Science* **348**, 1234 (2015)
8. M. Saliba, T. Matsui, K. Domanski, J.Y. Seo, A. Ummadisingu, S.M. Zakeeruddin, J.P. Correa-Baena, W.R. Tress, A. Abate, A. Hagfeldt, M. Grätzel, *Science* **354**, 206 (2016)
9. L. Liang, P. Gao, *Adv. Sci.* **5**, 1700331 (2018)
10. P. Chandra, S.K. Mandal, *Phys. B Condens. Matter* **625**, 413536 (2022)
11. B.W. Park, B. Philippe, X. Zhang, H. Rensmo, G. Boschloo, E.M.J. Johansson, *Adv. Mater.* **27**, 6806 (2015)
12. R.L.Z. Hoyer, R.E. Brandt, A. Osherov, V. Stevanovic, S.D. Stranks, M.W.B. Wilson, H. Kim, A.J. Akey, J.D. Perkins, R.C. Kurchin, J.R. Poindexter, E.N. Wang, M.G. Bawendi, V. Bulovic, T. Buonassisi, *Chem. A Eur. J.* **22**, 2605 (2016)
13. D. Kiermasch, P. Rieder, K. Tvingstedt, A. Baumann, V. Dyakonov, *Sci. Rep.* **6**, 1 (2016)
14. A. Suzuki, T. Ohtsuki, T. Oku, T. Akiyama, *Mater. Sci. Eng. B Solid State Mater. Adv. Technol.* **177**, 877 (2012)
15. R.S. Sanchez, V. Gonzalez-Pedro, J.W. Lee, N.G. Park, Y.S. Kang, I. Mora-Sero, J. Bisquert, *J. Phys. Chem. Lett.* **5**, 2357 (2014)
16. Y. Mateyshina, A. Slobodyuk, V. Kavun, N. Uvarov, *Solid State Ionics* **324**, 196 (2018)
17. M.R. Das, A. Mukherjee, P. Mitra, *Mater. Sci. Pol.* **35**, 470 (2017)
18. K. Ahmad, S.N. Ansari, K. Natarajan, S.M. Mobin, A.C.S. Appl. Energy Mater. **1**, 2405 (2018)
19. M. Venkateswarlu, K. Narasimha-Reddy, B. Rambabu, N. Satyanarayana, *Solid State Ionics* **127**, 177 (2000)
20. R.J. Sengwa, P. Dhatarwal, S. Choudhary, *Solid State Ionics* **324**, 247 (2018)
21. B. Harihara-Venkataraman, K.B.R. Varma, *Solid State Ionics* **167**, 197 (2004)
22. H. Yamamura, S. Takeda, K. Kakinuma, *J. Ceram. Soc. Japan* **115**, 471 (2007)
23. P. Maji, A. Ray, P. Sadhukhan, A. Roy, S. Das, *Mater. Lett.* **227**, 268 (2018)
24. R. Kaur, V. Sharma, M. Kumar, M. Singh, A. Singh, *J. Alloys Compd.* **735**, 1472 (2018)
25. R. Tang, C. Jiang, Y. Fang, H. Yang, *Mater. Technol.* **30**, A181 (2015)
26. B.H. Venkataraman and K.B.R. Varma, *Solid State Ionics* **167**, 197 (2004)
27. H. Yamamura, S. Takeda, and K. Kakinuma, *Solid State Ionics* **178**, 1059 (2007)
28. M.S. Sheikh, A.P. Sakhya, P. Sadhukhan, A. Dutta, S. Das, T.P. Sinha, *Ferroelectrics* **514**, 146 (2017)
29. T. Paul, A. Ghosh, *J. Appl. Phys.* **121**, 135106 (2017)
30. T. Okiba, K. Shozugawa, M. Matsuo, T. Hashimoto, *Solid State Ionics* **346**, 115191 (2020)
31. F.B. Abdallah, A. Benali, S. Azizi, M. Triki, E. Dhahri, M.P.F. Graça, M.A. Valente, *J. Mater. Sci. Mater. Electron.* **30**, 8457 (2019)
32. M.R. Anantharaman, K.A. Malini, S. Sindhu, E.M. Mohammed, S.K. Date, S.D. Kulkarni, P.A. Joy, P. Kurian, *Bull. Mater. Sci.* **24**, 623 (2001)
33. S.K. Badge, A.V. Deshpande, *Solid State Ionics* **334**, 21 (2019)
34. A.K. Jonscher, *Nature* **267**, 673 (1977)

Publisher's Note Springer Nature remains neutral with regard to jurisdictional claims in published maps and institutional affiliations.